Fully Reconfigurable Silicon Photonic Lattice Filters With Four Cascaded Unit Cells

Stevan S. Djordjevic, *Student Member, IEEE*, Lian Wee Luo, *Student Member, IEEE*, Salah Ibrahim, *Member, IEEE*, Nicolas K. Fontaine, *Student Member, IEEE*, C. B. Poitras, *Member, IEEE*, Binbin Guan, Linje Zhou, *Member, IEEE*, Katsunari Okamoto, *Fellow, IEEE*, Zhi Ding, *Fellow, IEEE*, Michal Lipson, *Fellow, IEEE*, and S. J. B. Yoo, *Fellow, IEEE*

***Abstract*—We present a fully reconfigurable optical filter built by cascading four identical unit cells. The devices are fabricated using two distinct methods: a complementary metal–oxide–semiconductor (CMOS) compatible process utilizes deep ultraviolet (DUV) lithography with tuning elements defined by ion implantation to make lateral p-i-n diodes for current injection regions, while an electron beam (E-beam) lithography process uses nickel chrome (NiCr) heaters as tuning elements. The fabricated devices are characterized using swept optical vector network analyzer (OVNA) coherent measurements.**

***Index Terms*—CMOS compatible photonics, photonic reconfigurable filters, silicon ring resonators.**

I. Introduction

SILICON photonics is a promising enabling technology for the future convergence of optical and electronic technologies on a single platform [1]. While optical waveguides have the capability of handling large bitrates and transporting multiple wavelengths at the same time [2], electronic circuits have the advantage in complex signal processing. However, a certain set of functions, such as filtering, correlation, multiplexing and similar, can be performed in the optical domain [3]–[5], at high bit rate, without involving electronics. Having a reconfigurable device that can perform several of these functions would be beneficial to the implementation of optical interconnects on multicore processors and memories. We present a lattice filter that can be dynamically reconfigured to potentially any transfer function, with order equal to the number of cascaded cells.

II. Fully Reconfigurable Lattice Filter

A lattice filter is built by cascading equal unit cells, therefore, the versatility and operability of the filter depends on the functionality of the unit cell [6], [7]. We present a highly versatile unit cell architecture, that can be configured to have any first order (one pole and one zero) transfer function [8], limited only by the maximum pole magnitude, which is determined by the waveguide propagation loss [9].

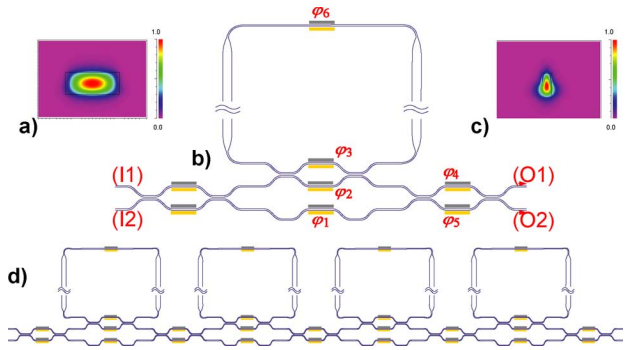

Fig. 1. (b) Unit cell structure. $(\mathrm{I}_1, \mathrm{I}_2)$ mark the two inputs to the cell and $(\mathrm{O}_1, \mathrm{O}_2)$ mark the outputs; $(\varphi_1 - \varphi_6)$ mark the phase shifting sections. The two unmarked phase shifting sections on the input side are not a part of the unit cell, but would belong to the previous unit cell in the cascaded implementation. (d) Four cascaded cells. TE mode structure of the ridge waveguides with 0.5-μm-thick silicon core: (a) 3-μm-wide waveguide, and (c) 0.5-μm-wide waveguide.

Fig. 1 shows the architecture of the unit cell in detail. Active tuning elements marked φ_1 to φ_6 represent the phase shifting sections. Since the change of phase is accompanied by a change of loss level in the case of free carrier injection [10], the general transfer function of the phase shifting section is:

$$R_i = \exp[(\alpha_i + j\Phi_i)\, L_i], \varphi_i = \Phi_i L_i \tag{1}$$

where L_i is the length of the section, $\alpha_i L_i$ is the excess generated loss, and φ_i is the induced phase change. Using these definitions, the transfer function of the unit cell is shown in equations (2a) and (2b) at the bottom of the next page, where

$$A(R_T, R_B) = \cos^2\theta \exp(R_T L) - \sin^2\theta \exp(R_B L) \tag{3a}$$

$$B(R_T, R_B) = j \sin\theta \cos\theta (\exp(R_T L) + \exp(R_B L)) \tag{3b}$$

$$C(R_T, R_B) = \cos^2\theta \exp(R_B L) - \sin^2\theta \exp(R_T L). \tag{3c}$$

In (3a)–(3c) R_T and R_B denote the complex transfer function related to the phase shifting sections in the upper ('top', R_T) and lower ('bottom', R_B) arm of the MZI's (that is, either (φ_3, φ_2) or (φ_5, φ_4) pair); finally, θ is the coupling coefficient of the directional coupler, set by the physical layer design (waveguide geometry, separation and the length of interaction).

The essential feature of the unit cell design can be inhered from (2b)–(2c). From the denominator, the magnitude of the pole depends only on φ_2 and φ_3 value, while the phase of the pole is determined solely by φ_6. From the numerator, the

Manuscript received August 26, 2010; revised October 11, 2010; accepted October 24, 2010. Date of publication November 09, 2010; date of current version December 22, 2010. This work was supported in part by the DARPA MTO SiPhaser project under Grant HR0011-09-1-0013.

S. S. Djordjevic, S. Ibrahim, N. K. Fontaine, B. Guan, L. Zhou, K. Okamoto, Z. Ding, and S. J. B. Yoo are with the Department of Electrical and Computer Engineering, University of California, Davis, CA 95616 USA (e-mail: sdjordjevic@ucdavis.edu; saibrahim@ucdavis.edu; nkfontaine@ucdavis.edu; sbyoo@ucdavis.edu).

L. W. Luo, C. B. Poitras, and M. Lipson are with the Cornell University, Ithaca, NY 14850-2824 USA.

Color versions of one or more of the figures in this letter are available online at http://ieeexplore.ieee.org.

Digital Object Identifier 10.1109/LPT.2010.2090868

1041-1135/$26.00 © 2010 IEEE

magnitude and phase of the zero are dependent on all six phases (φ_1 to φ_6). This means that the pole and the zero of the transfer function can be set independently, since after setting the pole value with $(\varphi_2, \varphi_3, \varphi_6)$ there is enough degrees of freedom $(\varphi_5, \varphi_4, \varphi_1)$ to set the value of zero. This is the key property of the design, allowing the unit cell to have any first order transfer function.

A lattice filter consisting of four cascaded unit cells is shown in Fig. 1(d). Since each of the unit cells can be configured separately, the filter can have any arbitrary transfer function of the fourth order.

III. Physical Layer Design

The device is designed for implementation on silicon-on-insulator (SOI) material platform. Two types of silicon rib waveguides are used: the 3.0 μm wide waveguide with the effective index of 3.263 and modal effective area of 1.028 μm^2 and the 0.5 μm wide waveguide with the effective index of 3.076 and modal effective area of 0.384 μm^2. Fig. 1(a) and (c) show the modal structure of the two waveguides. The wide waveguide shown in Fig. 1(a) has lower scattering loss due to lower confinement of the mode and is used for main sections of the ring resonator to allow for high Q-factor. Using 200 μm long parabolic tapers, the 3.0 μm wide waveguide is tapered adiabatically to the 0.5 μm waveguide, shown in Fig. 1(c). The narrow waveguide has smaller minimum bending radius, stronger evanescent tails and smaller effective area and is therefore used for central MZI waveguides, directional couplers and phase shifting sections. The gap of the directional coupler is 0.5 μm. To allow for fabrication tolerances, devices with different values of directional coupler lengths (6.5 μm to 27.5 μm with 3 μm increment) are fabricated on the same die. Ring resonator circumference is 8064 μm, providing free spectral range (FSR) of 10 GHz. All waveguides have bending radii larger then 300 μm to minimize the bending loss.

IV. Fabrication Process

The first batch of devices was fabricated at the University of California Microlab facility. Fabrication process starts with 6'' SOI wafers with buried oxide (BOX) layer thickness of 3 μm and top silicon layer of 0.5 μm. First, 120 nm thick low temperature oxide (LTO) is deposited as a hard etching mask. The waveguide layer is defined using DUV ASML stepper 5:1 reduction camera with 248 nm krypton fluoride (KrF) laser. After post exposure bake and developing, the defined photoresist pattern is heated to induce the photoresist reflow, reducing the roughness of the photoresist structure by smoothing the sidewalls under surface tension. The photoresist pattern is transferred to the hard mask using oxide etcher (LAM2) and from the hard mask to the silicon layer using highly anisotropic dry etching system (LAM5). The etching depth is 250 nm. Next, the wafers have undergone wet thermal oxidation, further reducing sidewall roughness remaining after dry etching. Lateral *p-i-n* diodes for current tuning sections, 0.5 mm long, are defined by ion implantation. Next, 620 nm thick LTO cladding is deposited and densified at 900°C before contact vertical via openings are etched through. Aluminum electrodes are sputtered, followed by metal layer photolithography, metal wet etch and forming gas annealing at 400 C. Fig. 2(c) shows the finished chip sample.

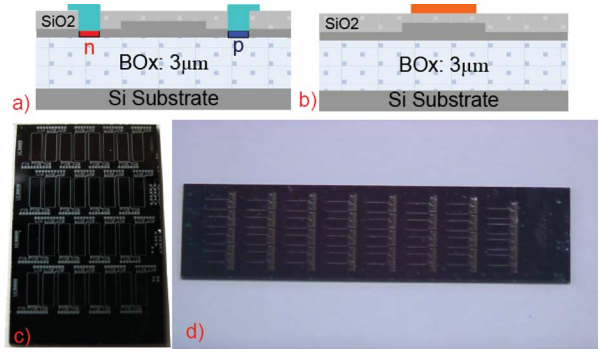

Fig. 2. (a) Cross-sections of DUV and (b) E-beam fabricated devices and (c) photographs of fabricated DUV and (d) E-beam samples. Total die sizes are approximately 21 mm × 14 mm (DUV sample) and 50 mm × 12 mm (E-beam sample).

The second batch of devices was fabricated at the Cornell University. The principal difference in the fabrication process, compared to the DUV process, is the use of electron beam (E-beam) writer as a lithographical tool and the utilization of thermo-optic effect in silicon, using nichrome heaters, as the mechanism for phase tuning. Fabricated chip sample is shown in Fig. 2(d).

V. Characterization of Fabricated Devices

The device transfer function for TE polarized light in 1.55 μm band is recorded by coherent interferometric measurement using the OVNA. The OVNA [11] includes a mode-hop-free swept laser signal split into the reference arm and the measurement arm including the device-under-test. The balanced detection of the coupled two signals provides the signal in the electrical domain. As Fig. 3 indicates, this allows retrieval of the amplitude and phase information of the transfer function s_{11}, s_{12}, s_{21} and s_{22} parameters. The quality factors (Q-factors) of filters, measured from the time domain impulse response are $\mathrm{Q_{DUV}} = 2.7 * 10^5$ for DUV fabricated device and $\mathrm{Q_{Ebeam}} = 8.5 * 10^5$ for the E-beam fabricated sample. These values correspond to waveguide losses of 2.0 dB/cm and 0.65 dB/cm, respectively. For DUV fabricated sample, with estimated coupling loss of 7 dB/facet (using positive tapers) and

$$T_{UC} = \begin{bmatrix} A(R_5, R_4)\, H & B(R_5, R_4) \exp(R_1 L) \\ B(R_5, R_4)\, H & C(R_5, R_4) \exp(R_1 L) \end{bmatrix} \tag{2a}$$

$$H = \frac{\exp(R_6 L)\left(B^2(R_3, R_2) - A(R_3, R_2)\, C(R_3, R_2)\right) + C(R_3, R_2)}{1 - A(R_3, R_2) \exp(R_6 L)} \tag{2b}$$

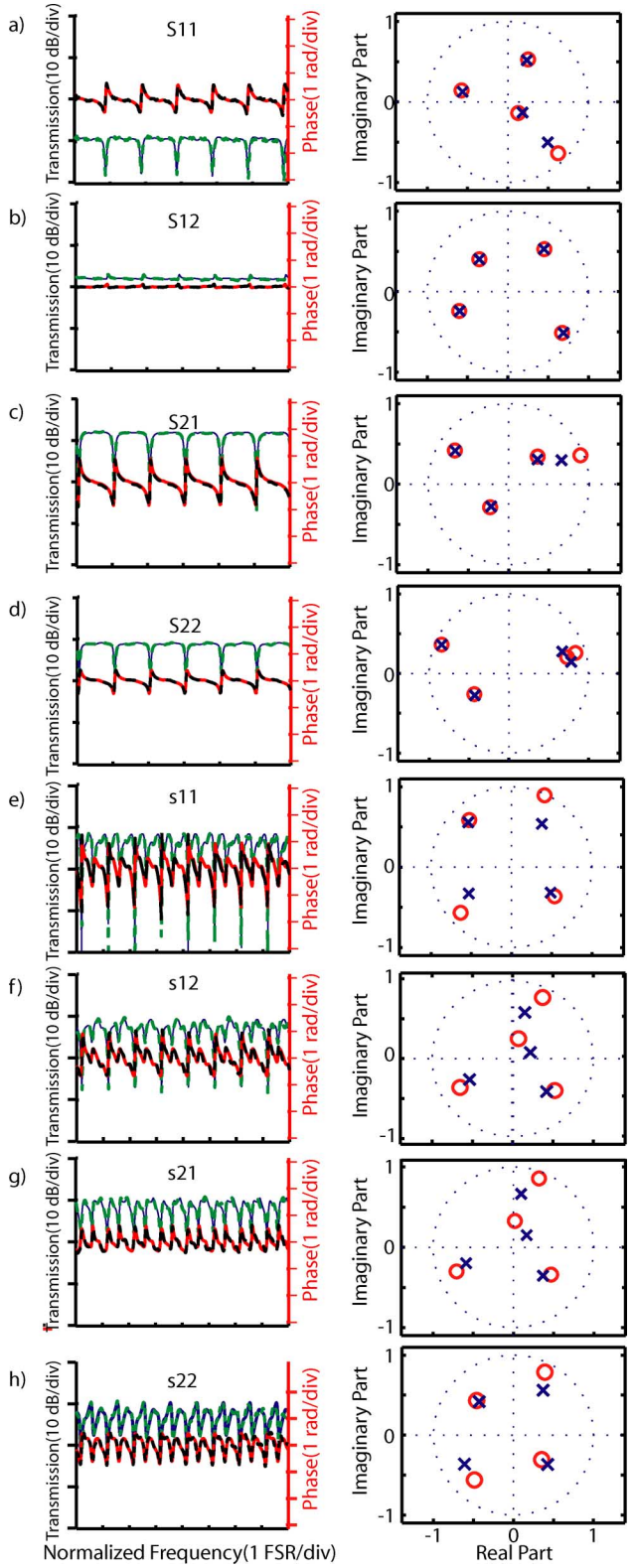

Fig. 3. (a) Measured amplitude (blue line) and phase (red line) of the DUV fabricated device s_{11}, (b) s_{12}, (c) s_{21}, and (d) s_{22} and (e) E-beam s_{11}, (f) s_{12}, (g) s_{21}, and (h) s_{22} parameter. Dashed lines are fitting curves. On the right-hand side of the plot, the respective position of the poles (blue crosses) and zeros (red circles) within the unit circle are marked.

measured insertion loss of 42 dB, approximate loss per stage is 7 dB. For E-beam fabricated sample, with estimated coupling loss of 3 dB (using inverse tapers) and measured insertion loss of 22 dB, approximate loss per stage is 4 dB.

Fig. 3 left column shows the measured curves in solid and fitted curves in dashed lines. The right column shows pole and zero values extracted from the curve fit. The values of poles and zeros in many cases are equal, which, from (2b), suggests that the initial phases of the MZI arms are equal and the splitting ratio of the directional couplers is 50%–50%. This reduces the transfer function to first order as in Fig. 3(c), or almost all-pass, zero order function, as in Fig. 3(b). After the amplitude and phase transfer function is known and the initial values of poles and zeros are retrieved by fitting the theoretical model to the measured spectra, the tuning elements are engaged using programmed training sequences, while monitoring the trajectories of poles and zeros continuously; measurements indicate that injected current of 11 mA induces 2π phase shift in the active element. This, together with the recursion algorithm, allows the mapping of desired pole and zero positions (corresponding to the targeted filter design) to the set of values of currents or voltages applied to the tuning elements. Algorithm design for the generation of arbitrary filters using the presented lattice filter will be the subject of a future publication.

VI. Conclusion

We have designed, fabricated and characterized four cascaded unit cell silicon lattice filters using two fabrication techniques. Future work will focus on tuning the devices to optical filter configurations, based on zero and pole positions.

References

[1] J. Orcutt and Khilo, "Demonstration of an electronic photonic integrated circuit in a commercial scaled bulk CMOS process," in *Proc. Conf. Lasers and Electro-Optics, 2008 and 2008 Conf. Quantum Electronics and Laser Science (CLEO/QELS 2008)*, 2008, pp. 1–2.

[2] D. Miller, "Rationale and challenges for optical interconnects to electronic chips," *Proc. IEEE*, vol. 88, no. 6, pp. 728–749, Jun. 2000.

[3] K. Okamoto, K. Takiguchi, and Y. Ohmori, "16-channel optical add/drop multiplexer using silica-based arrayed-waveguide gratings," *Electron. Lett.*, vol. 31, pp. 723–724, 1995.

[4] E. Dowling and D. MacFarlane, "Lightwave lattice filters for optically multiplexed communication systems," *J. Lightw. Technol.*, vol. 12, no. 3, pp. 471–486, Mar. 1994.

[5] L.-W. Luo, S. Ibrahim, C. B. Poitras, S. S. Djordjevic, H. L. Lira, L. Zhou, J. Cardenas, B. Guan, A. Nitkowski, Z. Ding, S. Yoo, and M. Lipson, "Fully reconfigurable silicon photonic interleaver," in *Proc. 2010 Conf. Lasers and Electro-Optics (CLEO) and Quantum Electronics and Laser Science Conf. (QELS)*, 2010, pp. 1–2.

[6] I. Panahi, G. Kannan, L. Hunt, D. MacFarlane, and J. Tong, "Lattice filter with adjustable gains and its application in optical signal processing," in *Proc. 2005 IEEE/SP 13th Workshop Statistical Signal Processing*, 2005, pp. 321–326.

[7] B. Moslehi, J. Goodman, M. Tur, and H. Shaw, "Fiber-optic lattice signal processing," *Proc. IEEE*, vol. 72, no. 7, pp. 909–930, Jul. 1984.

[8] K. Jinguji, "Synthesis of coherent two-port optical delay-line circuit with ring waveguides," *J. Lightw. Technol.*, vol. 14, no. 8, pp. 1882–1898, Aug. 1996.

[9] C. K. Madsen and J. H. Zhao, *Optical Filter Design and Analysis: A Signal Processing Approach*, ser. Microwave and Optical Engineering. Hoboken, NJ: Wiley, pp. 108–114.

[10] Q. Xu, B. Schmidt, S. Pradhan, and M. Lipson, "Micrometre-scale silicon electro-optic modulator," *Nature*, vol. 435, pp. 325–327, Jan. 1, 2005.

[11] D. K. Gifford, B. J. Soller, M. S. Wolfe, and M. E. Froggatt, "Optical vector network analyzer for single-scan measurements of loss, group delay, and polarization mode dispersion," *Appl. Opt.*, vol. 44, pp. 7282–7286, 2005.